J. Fluid Mech., page 1 of 29. © Cambridge University Press 2012
doi:10.1017/jfm.2011.417

Direct numerical simulations of roughness-induced transition in supersonic boundary layers

Suman Muppidi and Krishnan Mahesh†

Aerospace Engineering & Mechanics, University of Minnesota, Minneapolis, MN 55455, USA

(Received 5 May 2011; revised 14 September 2011; accepted 21 September 2011)

Direct numerical simulations are used to study the laminar to turbulent transition of a Mach 2.9 supersonic flat plate boundary layer flow due to distributed surface roughness. Roughness causes the near-wall fluid to slow down and generates a strong shear layer over the roughness elements. Examination of the mean wall pressure indicates that the roughness surface exerts an upward impulse on the fluid, generating counter-rotating pairs of streamwise vortices underneath the shear layer. These vortices transport near-wall low-momentum fluid away from the wall. Along the roughness region, the vortices grow stronger, longer and closer to each other, and result in periodic shedding. The vortices rise towards the shear layer as they advect downstream, and the resulting interaction causes the shear layer to break up, followed quickly by a transition to turbulence. The mean flow in the turbulent region shows a good agreement with available data for fully developed turbulent boundary layers. Simulations under varying conditions show that, where the shear is not as strong and the streamwise vortices are not as coherent, the flow remains laminar.

Key words: boundary layer stability, compressible boundary layers, high-speed flow

1. Introduction

Transition of high-speed boundary layer flows significantly alters the aerodynamic drag and heat transfer, and affects the design of supersonic and hypersonic vehicles. For example, thermal protection system (TPS) design for hypersonic vehicles is strongly influenced by accurate prediction of when transition occurs (Berry *et al.* 2001). Transition at high speeds is affected by various factors such as Reynolds number, Mach number, surface temperature, pressure gradient, acceleration and surface roughness. Review articles by Tani (1969), Reshotko (1976), Saric, Reed & White (2003) and Federov (2010), among others, list the considerable work done on transition of incompressible and high-speed flows. Reviews by Reda (2002) and Schneider (2008) summarize existing knowledge of hypersonic transition on blunt bodies with roughness, with the focus being on reentry vehicles.

For given flow conditions, surface roughness is found to result in an early transition compared to smooth surfaces. Klebanoff & Tidstrom (1972) use flow past a two-dimensional roughness element to conclude that roughness does not introduce

† Email address for correspondence: mahesh@aem.umn.edu

disturbances in the boundary layer but rather destabilizes the flow, causing the existing disturbances to grow and become unstable; the roughness shape influences the level of destabilization and hence the speed of the resulting transition. Corke, Bar-Sever & Morkovin (1986) studied transition due to distributed roughness, and observed that low-inertia fluid in the valleys between roughness elements is far more susceptible to freestream disturbances than the fluid over smooth walls without local separations. Small roughness affects transition by changing the receptivity of the mean flow to existent disturbances, while large roughness distorts the flow enough to create locally separated flow and regions of turbulence, which then become a mechanism for exciting new boundary layer disturbance growth (Stetson 1990). Stetson also discusses the difficulty of classifying roughness due to the various parameters involved – roughness height, configuration, spacing, and whether the roughness is distributed or isolated, two-dimensional or three-dimensional.

Prediction of roughness-induced transition is often based on correlations like Re_θ/M_e obtained from experimental results. Reshotko (2007) concludes that this correlation neglects the effects of pressure gradient, roughness and surface temperature. Redford, Sandham & Roberts (2010) performed simulations to study transition over a three-dimensional roughness element. Their parametric study is used to arrive at a correlation that divides the transitional and laminar flows, and is based on roughness height Reynolds number, Mach number and wall temperature. Berry *et al.* (2001) list the different correlations used to design the shuttle orbiter and show that transition correlations are sensitive to the underlying computational methods. Note that these correlations are for flow past an isolated roughness element.

The broad paths to transition have been described by Morkovin, Reshotko & Herbert (1994). Small-amplitude roughness induces transition by the linear amplification of exponentially growing disturbances followed by secondary instabilities and breakdown to turbulence (Reshotko 2001). An increase in roughness height can result in bypass transition, a comparatively rapid process that bypasses the Tollmien–Schlichting (T–S) route. Transient growth theory has been studied as a candidate for bypass transition where the initial disturbance growth is algebraic and the modes are subcritical according to the T–S neutral curve (Reshotko 2001; Tumin & Reshotko 2003). Reshotko (2008) describes the failure of the T–S based explanation for three-dimensional roughness and proposes that transient growth theory is a more useful approach. Transient growth theory predicts that the optimal transient growth is associated with streamwise vortices (Tumin & Reshotko 2003; Choudhari & Fischer 2005), and streamwise vortices have been observed in roughness-induced transition (Van Driest & McCauley 1960; White 2002; Tumin & Reshotko 2004; Berry & Horvath 2007; Wang & Zhong 2008). However, the role of these vortices, and the mechanism of their generation, are not very clear.

For hypersonic flows, it has been shown that transition occurs earlier (at approximately a quarter of the transitional Reynolds number) for flows over distributed roughness patterns as compared to isolated roughness elements (Reda 2002). Transition due to distributed roughness has commonly involved arrays of discrete roughness elements. Van Driest & Blumer (1962) studied the effects of a circular array of spherical elements placed near the nose of a cone on its transition at Mach number 2.71. By varying the position of the roughness elements from the cone and the size of the elements, it was shown that the minimum trip size required to cause transition varied exponentially (fourth power) with the distance of the roughness element from the cone's apex. Ergin & White (2006) performed an experimental study of the unsteady (incompressible) flow behind a spanwise array

of cylindrical roughness elements. The results are interpreted as transition being a competition between the unsteady disturbance growth and the relaxation of the stabilizing steady flow. Choudhari & Fischer (2005) performed numerical simulations of transition on a flat plate boundary layer due to a spanwise array of cylindrical roughness elements (spaced three diameters away from each other). They observe that, at a large enough roughness height, the separated flow behind the element becomes spontaneously unsteady. Their simulations reveal a train of hairpin vortices similar to the observations by Acarlar & Smith (1987) for flow past a single hemispherical roughness element. While their paper addresses the role of spanwise proximity of roughness elements, Choudhari & Fischer (2005) propose that the role of streamwise proximity might be a more crucial aspect of transition due to distributed roughness. Choudhari *et al.* (2010) performed simulations of Mach 3.5 laminar flow past a single diamond-shaped roughness element, as well as two roughness elements in tandem (in the line of the freestream flow). It is shown that the flow is dominated by streaks, which leads to an earlier transition than predicted by linear stability theory of the underlying boundary layer. Wang & Zhong (2008) performed simulations of transient growth and receptivity on a Mach 6 flat plate due to a periodic three-dimensional roughness element. In their simulations, the boundary conditions on the rough surface are transferred to a smooth surface. It is shown that this is valid as long as the ratio of boundary layer thickness to roughness height is greater than 35, and the simulations show that the roughness introduces counter-rotating vortices and transient growth into the flow. Recent work on high-speed boundary layers over three-dimensional rough walls has focused on the effect of roughness on the turbulent boundary layer and not on transition; the incoming flow is turbulent (Ekoto *et al.* 2008; Sahoo, Papageorge & Smits 2010). The effect of distributed surface roughness on transition has been studied by Roberts & Yaras (2005) in the context of low-speed flow over turbine blades, and it is observed that roughness and freestream turbulence have comparable effects on transition location.

The objective of the present work is to study the mechanism of transition in supersonic boundary layers due to distributed roughness, using direct numerical simulations (DNS). Laminar flow over a flat plate (Mach 2.9) encounters a rough surface, and the effect of this roughness on the incoming laminar boundary layer is studied. The simulations provide detailed flow features as two-dimensional laminar flow develops unsteadiness and becomes turbulent. The results of the simulation show that roughness perturbs the laminar flow so as to create a strong shear, and also generates pairs of counter-rotating streamwise vortices. Interaction with these vortices causes the shear layer to break up and give rise to a flow that is fully turbulent. The paper is organized as follows. The algorithm is described in § 2, and the problem setup and computational details are described in § 3. Section 4.1 shows that the roughness-induced transition gives rise to a fully developed turbulent flow. Section 4.2 describes the evolution of the shear layer and the vortices and their interaction. Section 5 discusses the effect of roughness height and wall temperature on transitional behaviour.

2. Algorithm

The simulations use an algorithm developed by Park & Mahesh (2007) for solving the compressible Navier–Stokes equations on unstructured grids:

$$\frac{\partial \rho}{\partial t} = -\frac{\partial}{\partial x_k}\left(\rho u_k\right), \tag{2.1}$$

$$\frac{\partial \rho u_i}{\partial t} = -\frac{\partial}{\partial x_k}\left(\rho u_i u_k + p\delta_{ik} - \sigma_{ik}\right), \tag{2.2}$$

and

$$\frac{\partial E_T}{\partial t} = -\frac{\partial}{\partial x_k}\left\{\left(E_T + p\right)u_k - \sigma_{ik}u_i - Q_k\right\}, \tag{2.3}$$

where ρ, u_i, p and E_T are density, velocity, pressure and total energy, respectively. The viscous stress σ_{ij} and heat flux Q_i are given by

$$\sigma_{ij} = \frac{\mu}{Re}\left(\frac{\partial u_i}{\partial x_j} + \frac{\partial u_j}{\partial x_i} - \frac{2}{3}\frac{\partial u_k}{\partial x_k}\delta_{ij}\right), \tag{2.4}$$

$$Q_i = \frac{\mu}{(\gamma - 1)M_\infty^2 RePr}\frac{\partial T}{\partial x_i}, \tag{2.5}$$

after non-dimensionalization, where Re, M_∞ and Pr denote the Reynolds number, Mach number and Prandtl number, respectively.

The governing equations are discretized using a cell-centred finite volume scheme. Upon integration over the control volume, application of the Gauss theorem, and some rearrangement, the discrete governing equations may be written as

$$\frac{\partial \rho_{cv}}{\partial t} = -\frac{1}{V_{cv}}\sum_{faces}\rho_f v_N A_f, \tag{2.6}$$

$$\frac{\partial (\rho u_i)_{cv}}{\partial t} = -\frac{1}{V_{cv}}\sum_{faces}\left[(\rho u_i)_f v_N + p_f n_i - \sigma_{ik,f} n_k\right] A_f, \tag{2.7}$$

$$\frac{\partial (E_T)_{cv}}{\partial t} = -\frac{1}{V_{cv}}\sum_{faces}\left[(E_T + p)_f v_N - \sigma_{ik,f} u_{i,f} n_k - Q_{k,f} n_k\right] A_f, \tag{2.8}$$

where V_{cv} is the volume of control volume, A_f is the area of the face, n_i is the outward normal vector at the surface, v_N is the face-normal velocity, and $\boldsymbol{q}_{cv} = (\int_{cv} \boldsymbol{q}\, \mathrm{d}V)/V_{cv}$ is the volume average within the cell, where $\boldsymbol{q} = (\rho, \rho u_i, E_T)$ is the vector of conservative variables. The subscript f denotes interpolated values at each face of the control volume. Discretization of the governing equations involves reconstruction of the variables at the faces from the cell centre values, and the spatial accuracy of the algorithm is sensitive to this flux reconstruction. The simulations employ a modified least-squares method for this reconstruction, which can be shown to be more accurate than a simple symmetric reconstruction, and more stable than a least-squares reconstruction. The algorithm uses a novel shock-capturing scheme that localizes numerical dissipation to the vicinity of flow discontinuities – thereby minimizing unnecessary dissipation. The solution is advanced in time using a second-order explicit Adams–Bashforth scheme, as

$$q_j^{n+1} = q_j^n + \frac{\Delta t}{2}\left[3\mathrm{rhs}_j(\boldsymbol{q}^n) - \mathrm{rhs}_j(\boldsymbol{q}^{n-1})\right], \tag{2.9}$$

where rhs_j denotes the jth component of the right-hand side of (2.7), and superscript n denotes the nth time step. Further details are provided in Park & Mahesh (2007).

3. Computational details

The objective of the present simulations is to study the effect of surface roughness on the laminar to turbulent transition in supersonic flows. A schematic of the

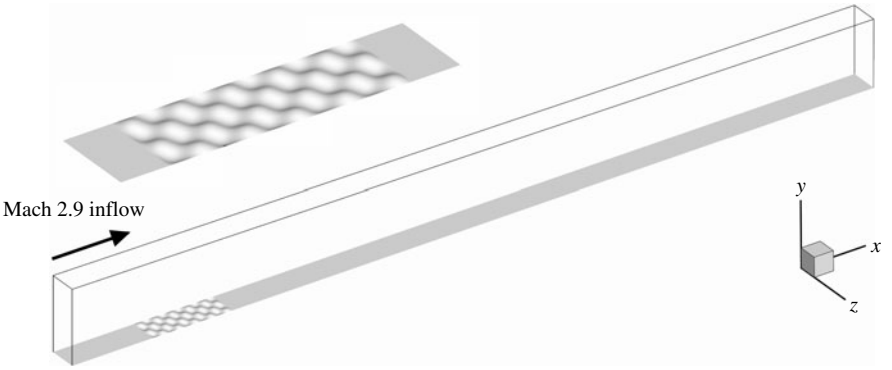

FIGURE 1. Schematic of the problem, showing the extent of the roughness strip along with the coordinate axes. The domain extends from $x = 4.0$ to $x = 9.0$ inches, 0.5 inches in the wall-normal direction, and 0.175 inches in the spanwise direction.

computational domain is shown in figure 1 along with the coordinate axes; x is the streamwise direction and y is the wall-normal direction. The length of the computational domain is 5 inches (127 mm), with the inflow at $x = 4.0$, the height and the spanwise extents are 0.5 and 0.175 inches (13 and 4.5 mm), respectively. The surface is defined as

$$\left.\begin{array}{ll} y_{wall} = k\sin(k_x x)\sin(k_z z), & \text{if } 4.5 < x < 5.0, \\ y_{wall} = 0, & \text{elsewhere,} \end{array}\right\} \tag{3.1}$$

where k is the peak roughness height, equal to 0.0075 inches (0.2 mm), and k_x and k_z are the wavenumbers in the streamwise and spanwise directions chosen such that the roughness region spans five full wavelengths in the streamwise direction and two in the spanwise direction. The domain is periodic in the spanwise direction. Incoming flow is laminar, at Mach 2.9 and with a freestream unit Reynolds number ($Re_\infty = \rho_\infty u_\infty / \nu_\infty$) of 635 000 per inch. A two-dimensional laminar boundary layer is specified at the inflow ($x = 4.0$) such that the boundary layer origin is at $x = 0$, based on the numerical similarity solution to the compressible boundary layer (Schlichting 1963). The boundary layer thickness at the inflow ($x = 4.0$) is ~0.022 inch (~0.6 mm), resulting in a $k/\delta_{inflow} \sim 0.35$ (and a $k/\delta_{x=4.5} \sim 0.30$, at the beginning of the roughness region). Zero-gradient boundary conditions are imposed at the outflow ($x = 9.0$), and freestream boundary conditions are imposed at the top boundary. At the wall, no-slip boundary conditions are implemented for the velocity, and a zero normal-derivative condition is imposed for pressure. The wall is kept at a constant temperature $T_{wall} = T_{stagnation}$, where $T_{stagnation} = [1 + \frac{1}{2}(\gamma - 1)M_\infty^2]T_\infty$. Sutherland's formula is used to compute viscosity as a function of the temperature ($T_{ref} = T_\infty = 170$ K, $C = 110$ K). The computational mesh used for the simulation consists of 36 million hexahedral elements, uniform in x and z, such that $\Delta x = 2.5 \times 10^{-3}$, $\Delta z = 9.1 \times 10^{-4}$ and $\Delta y_{min} = 5 \times 10^{-5}$ (all in inches). The roughness strip causes the laminar flow to transition, and at $x = 7.5$, where the flow is turbulent, the grid spacing in viscous wall units equals $\Delta x^+ = 15$, $\Delta z^+ = 5.4$ and $\Delta y^+_{min} = 0.3$. The computational mesh was arrived at after preliminary simulations on coarser meshes and a grid refinement study. Figure 2 shows the details of the computational mesh over the roughness element, on x–y and x–z planes, over one wavelength of the surface.

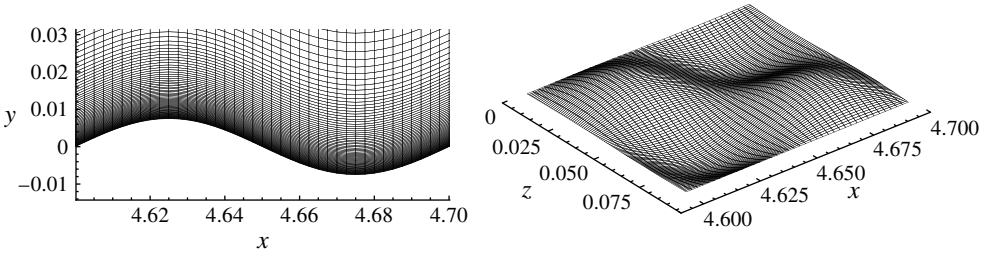

FIGURE 2. Computational mesh in the roughness region shown on side plane (x–y plane) and along the surface. The figure shows the mesh over one wavelength of the roughness surface.

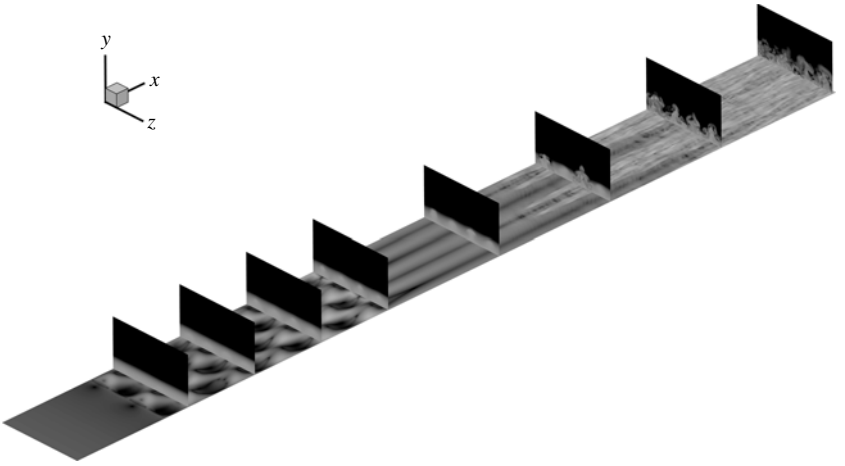

FIGURE 3. An instantaneous realization of the flow near the roughness strip, showing the transitional behaviour. The figure shows contours of magnitude of vorticity along the wall, and temperature on the end planes.

4. Solution

Figure 3 shows the instantaneous flow using contours of vorticity magnitude along the wall, and contours of temperature on y–z planes. The originally two-dimensional flow becomes three-dimensional as the roughness introduces spanwise velocity as well as spanwise gradients. Figure 4 shows instantaneous contours of density on an x–y plane and contours of streamwise velocity u on a wall-parallel plane at $y = 0.01$. Fluid decelerates upon approaching the roughness elements and travels around them. This has the effect of generating alternating streaks of high and low velocity, and a wake-like behaviour behind each row of roughness elements. Further downstream, the figure shows perturbations of the low-speed streaks, leading to transition. Visually, the flow appears to be turbulent past $x = 6.0$. Figure 4 also includes a closer view of the wall-parallel plane to show the transitional flow region in detail.

4.1. *Turbulent region*

Transition to turbulence is accompanied by an increase in both the drag and the heat transfer. Figure 5 plots the streamwise variation of $C_f = \tau_{wall}/(\rho_\infty u_\infty^2/2)$ and $q = -k\,\partial T/\partial y$. Here, q_0 is the heat flux upstream of the roughness region. The laminar region is characterized by low skin friction and heat transfer. Past the

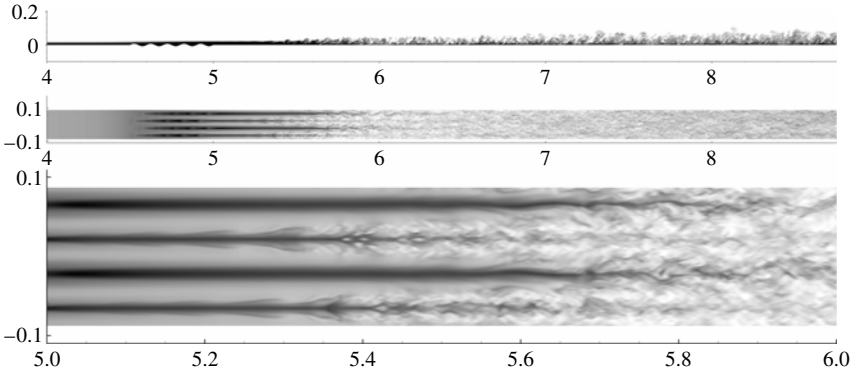

FIGURE 4. Contours of density on a side plane (x–y plane) and contours of streamwise velocity u on a wall-parallel plane (x–z plane, at $y = 0.01$), showing regions of laminar flow, transition and turbulent flow. The figure also shows the transitional region in detail.

end of the roughness strip ($x = 5.0$), both these quantities begin to rise, indicating unsteadiness and mixing, peak around $x = 6.0$, and thereafter exhibit a steady decrease, characteristic of turbulent boundary layers. Note that the turbulent heat flux is about five times that of the incoming flow. Figure 5 also compares C_f and q/q_0 with that of the similarity solution (Schlichting 1963) upstream of the roughness region. Note that the computational domain extends approximately $25\,\delta_{inflow}$ upstream of the roughness region. Both skin friction and heat transfer begin to diverge from the similarity solution past $x = 4.25$, approximately $12\,\delta_{inflow}$ from the domain inflow. This deviation is also observed in figure 5(c), which plots the wall-normal profiles of streamwise velocity at a few x locations upstream of the roughness region. Profiles show the deceleration of the near-wall fluid as it approaches the roughness elements.

Figure 6 shows the streamwise variation of Re_θ, where θ is the momentum thickness computed as

$$\theta = \int_0^\infty \frac{\rho(y)u(y)}{\rho_\infty u_\infty}\left(1 - \frac{u(y)}{u_\infty}\right) \mathrm{d}y. \tag{4.1}$$

Re_θ can be computed using either μ_{wall} or μ_∞, both of which are plotted in figure 6(a). Note that between $x = 6$ and 9, the Reynolds number varies between 1400 and 4000 (based on μ_∞). Figure 6(b) plots the skin friction coefficient C_f as a function of Re_θ based on μ_{wall} and compares to data from various sources, extracted from Loginov, Adams & Zheltovodov (2006). The available data show some scatter, and lie on either side of the predicted curve based on Van Driest II transformation. Loginov *et al.* (2006) mention that the scatter is comparatively higher at smaller Reynolds numbers, owing to the difficulty of obtaining developed turbulent boundary layers at these Reynolds numbers, also evidenced by fewer data points in this range. Note that the present data fall within the observed scatter. Figure 7 plots the variation of boundary layer thickness (defined as the wall-normal location where $u = 99\,\%\,u_\infty$ and normalized by δ at the end of the domain) and the shape factor $H = \delta^*/\theta$ as a function of the streamwise distance. Here δ^* is the displacement thickness computed as

$$\delta^* = \int_0^\infty \left(1 - \frac{\rho(y)u(y)}{\rho_\infty u_\infty}\right) \mathrm{d}y. \tag{4.2}$$

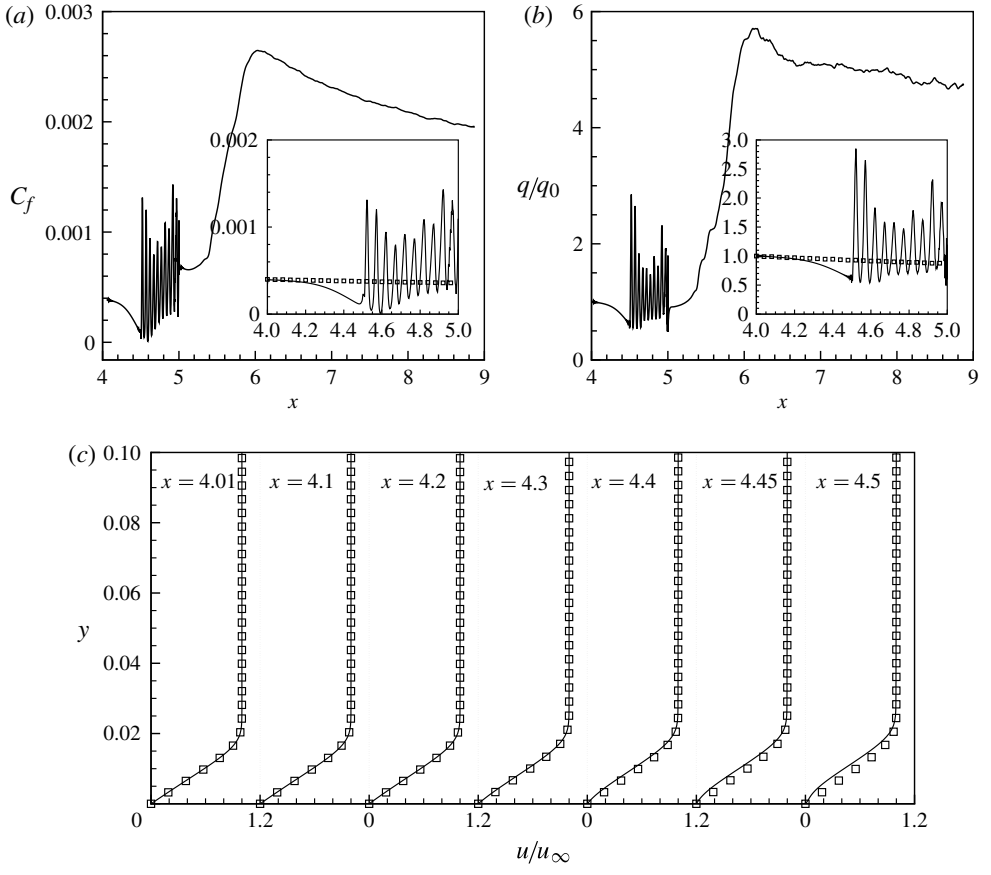

FIGURE 5. Variation of (*a*) skin friction coefficient and (*b*) heat transfer at the wall plotted as a function of the streamwise distance (q_0 is the heat transfer at $x = 4.0$). Note that the roughness region extends from $x = 4.5$ to $x = 5.0$ and the flow appears to transition downstream of the roughness strip. Inset: Comparison with predictions from the similarity solution (□). (*c*) Wall-normal profiles of mean streamwise velocity at a few locations between the domain inflow and the roughness region, compared to the similarity solution. The curves diverge starting at approximately $x = 4.3$, or $\sim 15\,\delta_{x=4.0}$ from the inflow.

Table 1 lists pertinent parameters of compressible turbulent boundary layer data (both experiments and simulations) used to validate the present results. The C_f in figure 5 and H in figure 7 show reasonable agreement with the reported values in table 1.

Figure 8 presents profiles of Van Driest transformed velocity as a function of the wall-normal distance at a few stations ($x = 6.5$, 7, 7.5, 8 and 8.5) along the streamwise distance. Van Driest velocity is computed as

$$u_{VD}(y) = \int_0^u \sqrt{\frac{\rho}{\rho_{wall}}}\,\mathrm{d}u, \tag{4.3}$$

and is plotted as a function of the wall-normal distance in wall units. The profiles are compared to existing numerical and experimental data. Note that the experimental data of Ringuette *et al.* (2009) comprise two curves: the open symbols correspond to the original data, and the filled symbols are obtained by 'shifting' the velocity profiles that fall below y^+ of 62. Details of the shifting process are provided in Ringuette

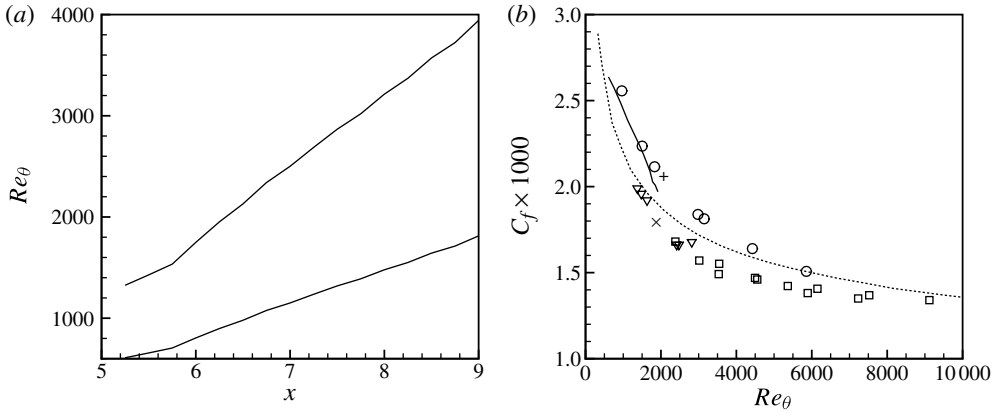

FIGURE 6. (*a*) Variation of Re_θ with the streamwise distance x. In the present simulations, $\mu_{wall} > \mu_\infty$ and hence Re_θ based on μ_∞ is higher. (*b*) Variation of C_f with Re_θ from the present simulation (continuous curve) along with available data (dashed curve and various symbols) from Loginov *et al.* (2006).

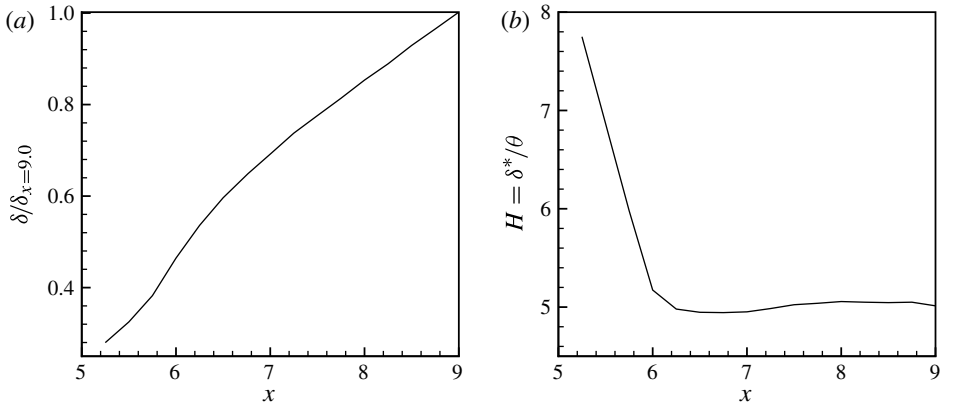

FIGURE 7. Variation of (*a*) boundary layer thickness δ based on $99\,\%\,u/u_\infty$ and (*b*) shape factor $H = \delta^*/\theta$ with the streamwise distance x. As the flow becomes turbulent, H decreases, and the values in the turbulent region agree reasonably with available data (reported in table 1).

et al. (2009). The experimental data of Zheltovodov *et al.* (1990) are taken from Loginov *et al.* (2006). The open symbols in this case correspond to the original data, and the filled symbols were obtained by scaling the dimensional experimental data with the friction velocity of the large-eddy simulation by Loginov *et al.* (2006). The DNS data of Wu & Martin (2007) have been extracted from Ringuette *et al.* (2009). Figure 9 presents comparisons of additional quantities using data from Bookey *et al.* (2005), Ringuette *et al.* (2009) and those reported in Loginov *et al.* (2006). Profiles of streamwise velocity u, density ρ, temperature T and Mach number M are plotted against y/δ, δ being the local boundary layer thickness (based on $99\,\%\,u/u_\infty$). The agreement is reasonable.

Reynolds stresses computed from the simulation are validated against available data. Figure 10(*a*) shows the density-weighted intensities $(\overline{\rho}/\overline{\rho}_{wall})\overline{u_i'u_j'}/u_\tau^2$ compared

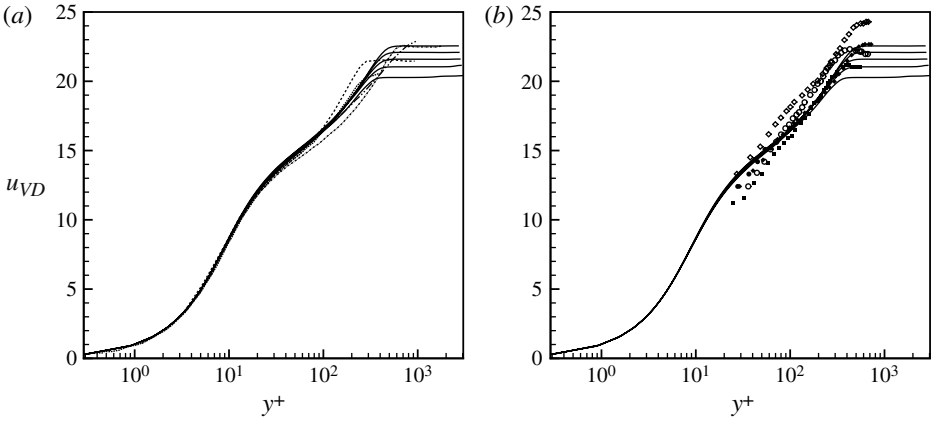

FIGURE 8. Comparison of Van Driest transformed velocity profiles at $x = 6.5$, 7, 7.5, 8 and 8.5 (continuous curves) compared to available data for turbulent boundary layers. (*a*) Comparison with simulations: dotted, Guarini *et al.* (2000); double dot-dashed, Gatski & Erlebacher (2002); dashed, Wu & Martin (2007); and dot-dashed, Loginov *et al.* (2006). (*b*) Comparison with experimental data: ■, Bookey *et al.* (2005); ●, ○, Ringuette *et al.* (2009); and ♦, ◇, Zheltovodov *et al.* (1990). The open symbols correspond to 'uncorrected' measurements (see text for details).

Reference	Mach number	Re_θ	C_f	Shape factor H
Guarini *et al.* (2000)	2.50	1577	0.002 82	
Gatski & Erlebacher (2002)	2.25	4250		
Loginov *et al.* (2006)	2.95	2046	0.002 05	5.19
Wu & Martin (2007)	2.90	2400	0.002 17	4.74
Bookey *et al.* (2005)	2.90	2400	0.002 25	5.51
Ringuette *et al.* (2009)	2.90	2400	0.002 17	5.49
Zheltovodov *et al.* (1990)	2.95	1826	0.001 79	5.30

TABLE 1. Relevant parameters of simulations and experiments whose mean flow data are compared to the present turbulent boundary layer in figures 8–10.

to results of simulations by Spalart (1998), Gatski & Erlebacher (2002) and Loginov *et al.* (2006). Loginov *et al.* (2006) use Favre averages. Figure 10(*b*) shows the comparison of velocity intensities $\overline{u_i'u_j'}/u_\tau^2$ as a function of y/δ with experiments by Klebanoff (1955) and Elena, Lacharme & Gaviglio (1985) and DNS of Spalart (1998) and Guarini *et al.* (2000). The data from Elena *et al.* (1985), Guarini *et al.* (2000), Gatski & Erlebacher (2002) and Loginov *et al.* (2006) are at similar Mach numbers, while those of Klebanoff (1955) and Spalart (1998) correspond to incompressible boundary layers. There are two curves for $\overline{u'u'}$ from the experiment of Elena *et al.* (1985), corresponding to one-component laser Doppler velocimetry (LDV) and two-component LDV. Figure 10(*a*,*b*) both show that the present results fall within the scatter observed in the available data. The detailed comparisons presented in this section make the point that, in the present simulations, the roughness region results in a laminar to turbulent transition, and a fully developed turbulent flow that compares reasonably with existing results for turbulent boundary layers.

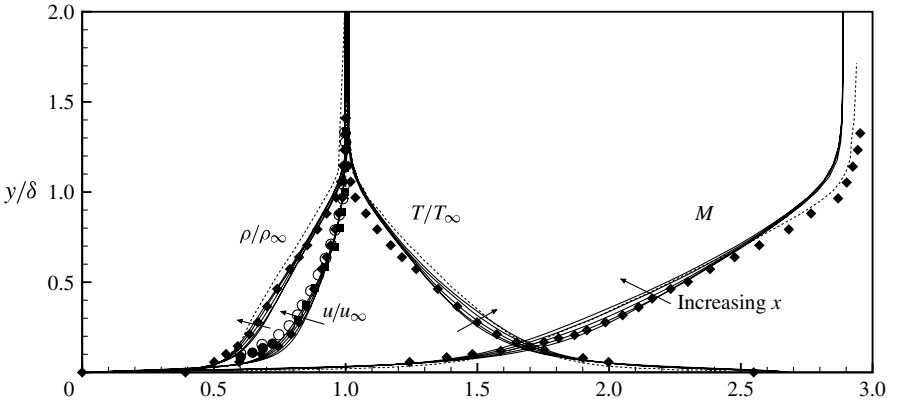

FIGURE 9. Profiles of density, streamwise velocity, temperature and Mach number from the present simulations plotted at $x = 6.5$, 7. 7.5, 8 and 8.5 (continuous curves), and compared to other results: - - - -, Loginov *et al.* (2006); ■, Bookey *et al.* (2005); ♦, Zheltovodov *et al.* (1990); and ●, Ringuette *et al.* (2009).

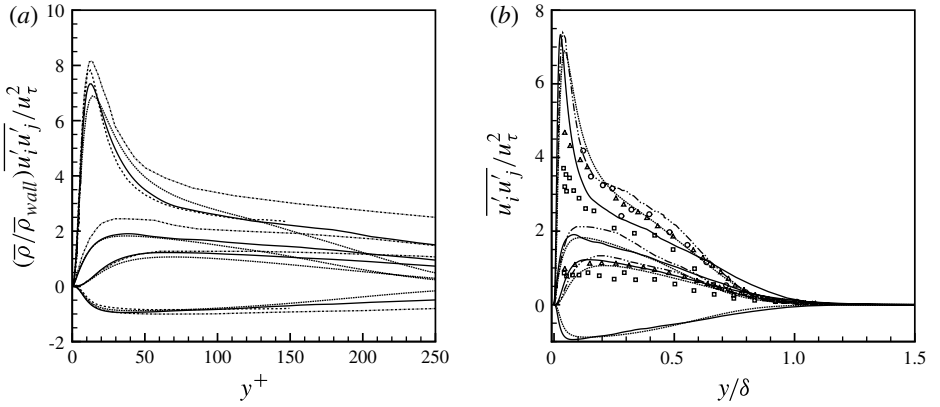

FIGURE 10. (*a*) Profiles of density-weighted Reynolds stress at $x = 8.5$ as a function of y^+ (continuous curve) compared to other results: dashed, Loginov *et al.* (2006); dot-dashed, Gatski & Erlebacher (2002); and dotted, Spalart (1998). (*b*) Turbulent intensities at $x = 8.5$ plotted as a function of y/δ (continuous curve) compared to other results: dotted, Spalart (1998); double dot-dashed, Guarini *et al.* (2000); ○, one-component LDV, and □, two-component LDV, both Elena *et al.* (1985); and ∇, Klebanoff (1955).

4.2. *Transition to turbulence*

This section describes the flow prior to becoming turbulent, in an attempt to understand the mechanism of transition. Flow past the roughness region is characterized by deceleration of the near-wall fluid, and the formation of a shear layer over the roughness elements. Underneath this shear layer, coherent pairs of streamwise vortices are observed, located in front of, and above, the individual roughness elements. Figure 12 shows contours of streamwise velocity u on a few y–z planes spanning the length of the roughness region. The figure shows only part of the wall-normal extent, and the plane-to-plane distance is not to scale. Flow around the first row of elements is qualitatively similar to the flow past a single roughness

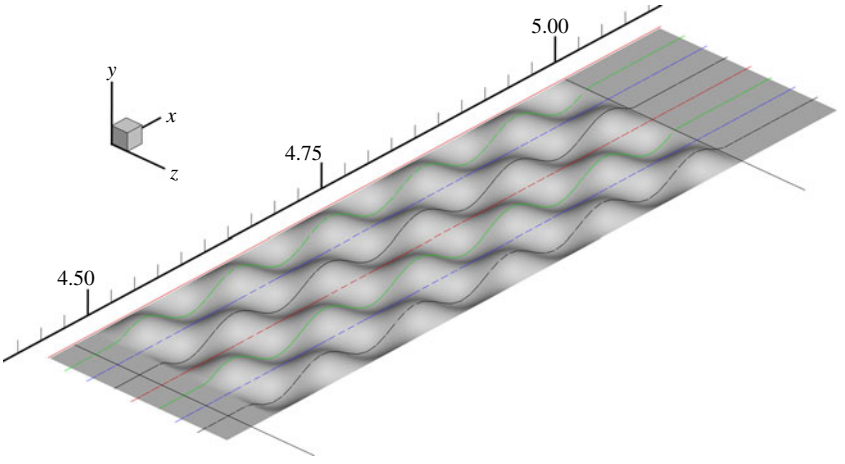

FIGURE 11. (Colour online available at journals.cambridge.org/flm) Schematic showing the location of the profiles plotted in figures 12 and 13.

element. Fluid slows down in front of the roughness elements, and travels around them. The successive roughness elements see not a uniform flow but a flow similar to the wake behind a wall-mounted obstacle. This results in decelerated flow in the line of the roughness elements, and accelerated flow in between the roughness elements. The troughs in the roughness region are characterized by low-momentum fluid whose volume appears to increase with increasing streamwise distance. Figure 12 also shows velocity profiles corresponding to a few streamwise and spanwise locations. At each x, u–y profiles are plotted at eight spanwise locations spaced $0.25\,(1/k_z)$ apart, as indicated in figure 11. These profiles show the progressive deceleration of the near-wall fluid. The resulting velocity profile over the line of roughness elements is closer to that of a mixing layer, as evidenced by a steep velocity gradient $(\partial u/\partial y)$ away from the wall. Note that the velocity profile is now inflectional, lending itself to instability. Profiles of near-wall fluid in between the roughness elements show progressive acceleration with increasing downstream distance. This non-uniformity in the spanwise direction produces significant spanwise gradients $(\partial u/\partial z)$.

The cumulative effect of the roughness strip on the incoming laminar flow is shown in figure 13, which compares the velocity fields before and after the roughness region using wall-normal profiles. The spanwise locations of these profiles, and the colour/greyscale scheme, are consistent with figure 11. Near-wall fluid slows down and the magnitudes of wall-normal and spanwise velocity components increase, as do the magnitudes of ω_x and ω_y. The profile of ω_z no longer resembles that of a boundary layer. Instead, it shows a peak in vorticity away from the wall corresponding to the steep gradient in the u profile. The velocity field is highly non-uniform in the spanwise direction, as indicated in figure 14, which shows contours of u, v, ω_x and ω_z on the plane at the end of the roughness region ($x = 5.0$). The contours of v and ω_x show pairs of fairly coherent streamwise vortices behind the roughness elements. Note that streamwise vortices have the effect of transferring low-momentum fluid away from the wall, as reflected by the contours of u. The ω_z contours show that there is a region of high (negative) vorticity in line with the roughness elements and away from the wall, consistent with the profiles seen in figure 13. Figure 15 shows a closer view

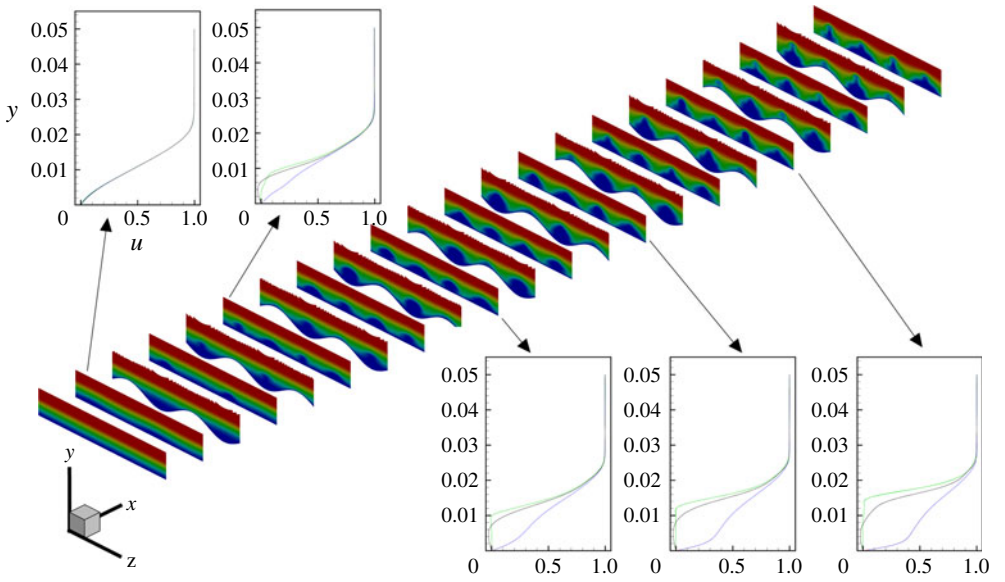

FIGURE 12. (Colour online) Contours and wall-normal profiles of streamwise velocity at a few planes ($x = 4.5$, 4.6, 4.7, 4.8 and 4.9) over the roughness region. The profiles show progressive deceleration of the near-wall fluid and a steepening of the velocity gradient. Note that profiles are plotted at eight spanwise locations indicated in figure 11. In all the figures, high-magnitude contours are shown in red, and the low-magnitude contours are shown in blue.

of the streamwise velocity contours along with vectors that indicate in-plane velocity (v, w), as well as the in-plane gradients of streamwise velocity ($\partial u/\partial z$ and $\partial u/\partial y$). The velocity profiles (figure 13) indicate a mixing-layer-like behaviour. Figure 15 shows that the mixing layer is not planar, but curved, from the fact that the spanwise and wall-normal velocity gradients are comparable. Note that the location of this shear layer $y \sim 0.02$ is greater than the peak roughness height $k = 0.0075$, and closer to the incoming boundary layer thickness. The velocity vectors show the rotation associated with the streamwise vortex pair behind the roughness element, and beneath the shear layer. The nature of the vortices and their role in transition will be visited in the following sections.

The steady inflow becomes unsteady past the roughness strip. Figure 16 identifies the origins of this unsteadiness, which ultimately results in the transition to turbulence. Along the streamwise distance x, peak turbulent intensities ($\overline{u'u'}$, $\overline{v'v'}$ and $\overline{w'w'}$) and the turbulent kinetic energy ($\overline{u_i'u_i'}$) on the y–z planes are plotted as functions of x. The unsteadiness begins to rise towards the end of the roughness region, exhibits two distinct peaks and decreases gradually thereafter. Note that the two peaks correspond to two different spanwise locations, and reflect the staggered arrangement of the roughness elements. Note that the streamwise locations of peak $\overline{v'v'}$ and $\overline{w'w'}$ appear to lag slightly the location of peak $\overline{u'u'}$. Figure 16 also shows the y location of the maximum $\overline{u'u'}$ as a function of x. In the turbulent region of the flow ($x \geqslant 6.0$), peak intensities are observed close to the wall – a feature of turbulent boundary layers and consistent with figure 10. Before the flow becomes turbulent, however, peak unsteadiness is observed away from the wall, $y \sim 0.02$. Turbulent intensities for developed boundary layers follow the relation $u_{rms} > w_{rms} > v_{rms}$, and this is indeed

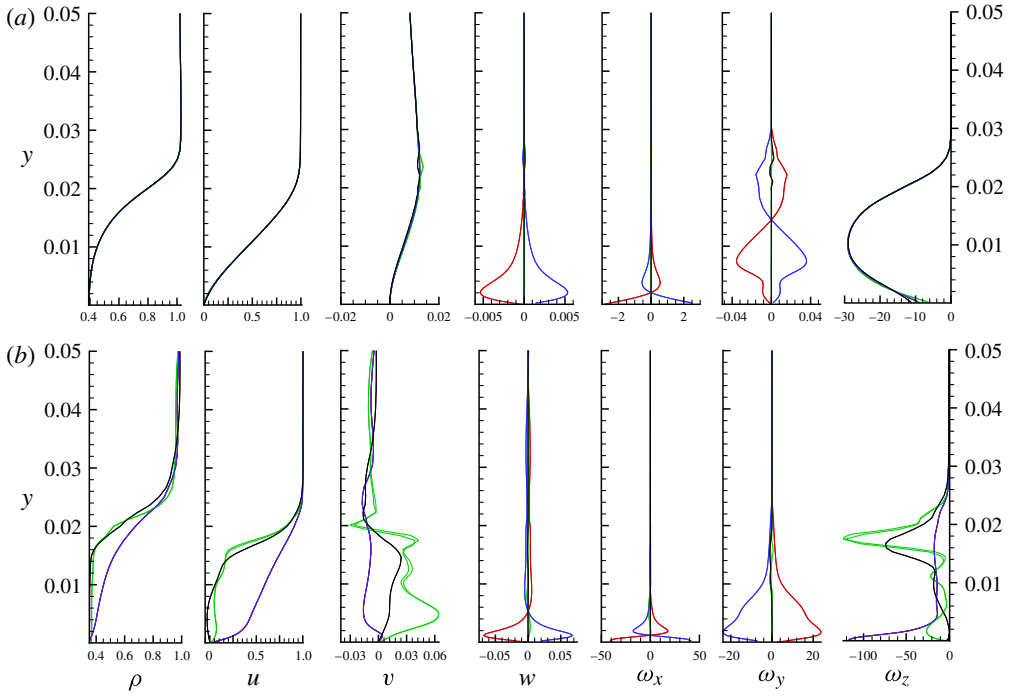

FIGURE 13. (Colour online) Instantaneous vertical profiles of density, velocity and vorticity (*a*) upstream ($x = 4.475$) and (*b*) downstream ($x = 5.0$) of the roughness region. The velocity profile is more indicative of a mixing layer than a boundary layer.

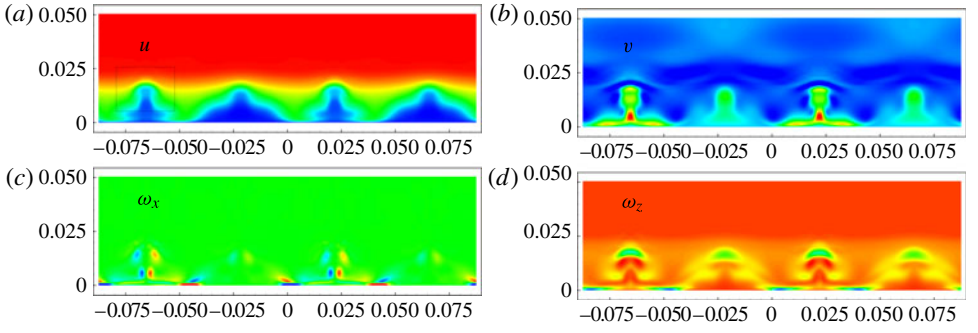

FIGURE 14. (Colour online) Velocity field at the end of the roughness region ($x = 5.0$) using contours of (*a,b*) streamwise and wall-normal velocities, u, v, and (*c,d*) streamwise and spanwise vorticities, ω_x, ω_z. A closer view is provided in figure 15.

true of figure 16 in the turbulent region. However, upstream of the turbulent region, peak $\overline{v'v'}$ and $\overline{w'w'}$ are very close to each other, and smaller than the peak $\overline{u'u'}$. This indicates a rotational motion in the y–z plane, or the unsteady behaviour of the streamwise vortices.

The velocity profiles indicated a shear layer that is lifted away from the wall, and the contours show that this shear layer is curved. The y location of the shear layer is consistent with the locations of peak unsteadiness upstream of the turbulent flow

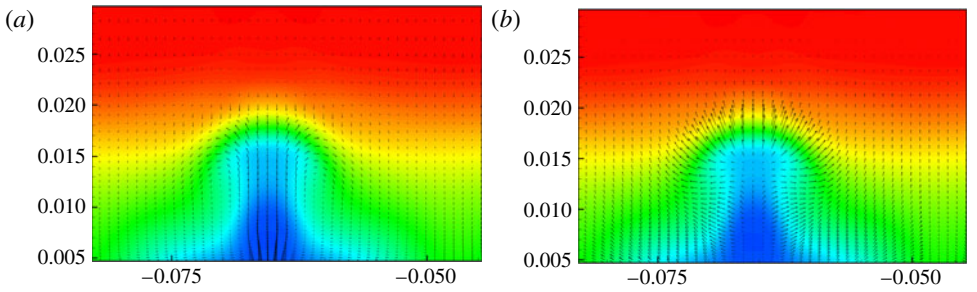

FIGURE 15. (Colour online) A closer view of the roughness wake at $x = 5.0$ using contours of streamwise velocity u. Vectors on the left indicate in-plane velocity field $(w,\ v)$, and vectors on the right indicate velocity gradients $(\partial u/\partial z,\ \partial u/\partial y)$. The gradients are comparable, indicating a curved mixing layer, and $(v$–$w)$ vectors show a pair of coherent vortices beneath the curved mixing layer.

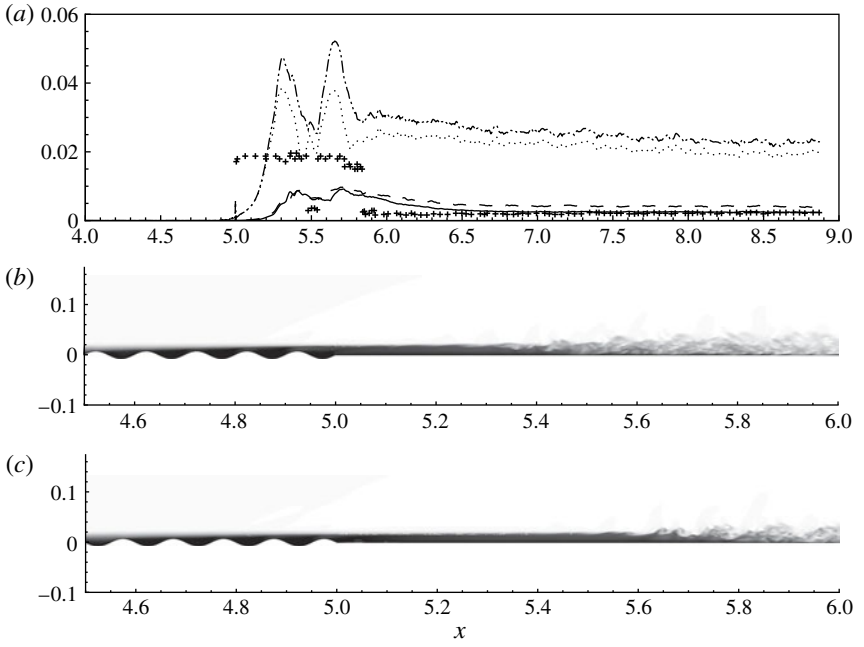

FIGURE 16. (a) Maximum turbulent intensities across z–y planes plotted as a function of x: double dot-dashed, $\overline{u_i' u_i'}$; dotted, $\overline{u'u'}$; full, $\overline{v'v'}$; and dashed, $\overline{w'w'}$. Symbols (+) show the wall-normal location of the maximum $\overline{u'u'}$. (b,c) Snapshots of the flow using contours of u on x–y planes corresponding to the peak $\overline{u'u'}$ in (a). Shear layer roll-up is observed at $y \sim 0.02$, consistent with the peak velocity gradients in figures 13 and 15, and supports (a).

region. Figure 16 further supports the notion that transition is due to the instability of the shear layer using contours of streamwise velocities on x–y planes in line with the roughness elements. Note that the shear layer begins to break up at streamwise locations corresponding to figure 16(a), and that this unsteadiness bears resemblance to a Kelvin–Helmholtz roll-up.

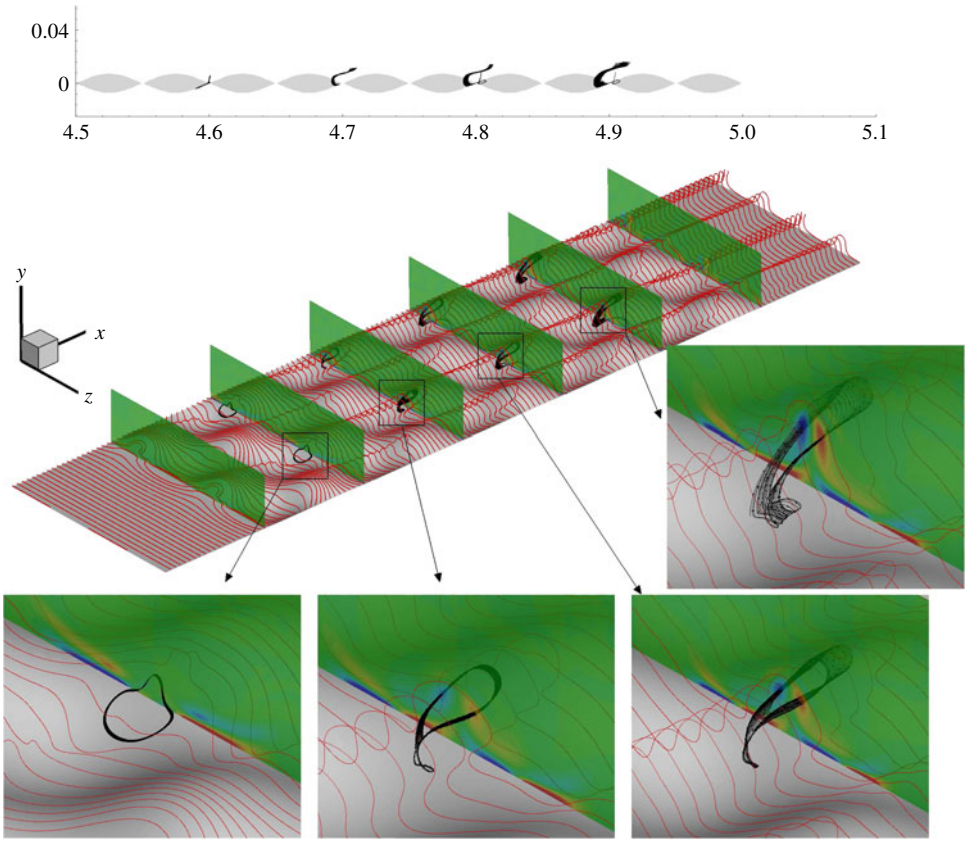

FIGURE 17. (Colour online) Vortex lines show the lifted shear layer and the streamwise vortices underneath. The red/grey vortex lines are released at the same wall-normal height on the spanwise boundary. The black vortex lines are released at the vortex cores on the z–y planes shown. The top panel shows the vortices in relation to the size of the roughness element.

4.3. *What role do the streamwise vortices play?*

The simulation results show that the roughness geometry perturbs the vorticity field in a manner that produces (a pair of) streamwise vortices in front of, and over, the roughness elements. With successive roughness elements (increasing x), these vortices appear to become longer and stronger, and are located farther away from the wall. The orientation of these vortices results in an upwash between them. While the streamwise vortices are steady earlier on, they then become unsteady and shed periodically downstream. Over the roughness region, these vortices are located under the shear layer. As they shed and move downstream, their mutually induced velocity is away from the wall, and they travel towards the shear layer. The interaction between the vortices and the shear layer is accompanied by a quick transition to turbulence. This section examines the nature of these vortices.

The vorticity field near the roughness region is illustrated in figure 17, which shows the roughness surface, a few end planes showing contours of streamwise vorticity ω_x and a few three-dimensional vortex lines. The red/grey vortex lines are released at the same wall-normal location ($y \sim 0.005$) along the spanwise boundary. The black vortex lines are released at the vortex cores observed on the end planes. The incoming

boundary layer only has spanwise vorticity, and hence the vortex lines are straight lines oriented in the $-z$ direction. Roughness has the effect of folding and lifting up the vortex sheet, and the vortex lines are consistent with the formation of the curved shear layer over the roughness elements first seen in figure 14. The black vortex lines show the evolution of the roughness-generated vortices. Earlier on, the vortex lines indicate $\omega_y \gg \omega_x$, and are located in front of the roughness elements. With increasing x, the vortex lines are observed farther from the wall, and farther upstream of the roughness elements. The vortices are predominantly oriented in the x direction with some inclination to the surface, which can be explained as a consequence of their mutually induced upward velocity. The vortices also appear to come closer to each other. The figure also shows the extent of the vortices in relation to the size of the roughness elements.

Streamwise vorticity behind roughness elements and obstacles has been discussed in past work. Mason & Morton (1987) use channel flow experiments and numerical simulations to study the generation of trailing vortices in the wakes of surface-mounted obstacles. They observe that symmetric obstacles generate pairs of dominant streamwise vortices in the wake, and that the sense of their rotation depends on the shape of the obstacles. It is shown that obstacles that divide the stream result in a central downwash, while obstacles that lift the flow over their crests produce vortex pairs with a central upwash. In the present case, the roughness elements have a smaller height compared to their spanwise extent, resulting in a flow that is lifted over the element, and the pair of streamwise vortices generated have a central upwash sense of rotation. A consequence of this orientation is the transport of low-momentum near-wall fluid (located between the vortices) away from the wall and towards the shear layer, further steepening the velocity gradient $\partial u/\partial y$. Trailing vortices as described by Acarlar & Smith (1987) have the opposite sense of rotation, and are understood to be formed by the boundary layer vorticity wrapping around the roughness element (creating a horse-shoe vortex whose legs form the counter-rotating vortex pair). Tumin & Reshotko (2003) study transient growth in compressible boundary layers and show that the optimal perturbations are associated with streamwise vortices. Reshotko & Tumin (2004) use transient growth theory to show that the optimal spanwise wavelengths are from 3 to 3.5 boundary layer thicknesses. Visually, figure 19 indicates the spanwise wavelength of the streamwise vortices to be 0.0875 inches ($\sim 4\delta_{x=4.0}$ or $\sim 3.5\delta_{x=4.5}$), and is the same as the spanwise wavelength of the roughness distribution. Interestingly, the streamwise vortices in the simulation are a result of the nonlinear roughness-induced boundary layer separation, and not necessarily optimal perturbations to the background boundary layer.

Figure 18 shows contours of streamwise velocity u and in-plane velocity vectors $(v,\ w)$ on end view planes spaced over a full wavelength $(1/k_x)$ of the roughness surface, between $x = 4.86$ and $x = 4.95$. The sequence of images show the origin and development of one pair of counter-rotating vortices. Figure 18(*a–c*) show the trough on the left becoming deeper, and the vectors show some streamwise vorticity. The sense of rotation of these vortices is to induce an upwash via their mutual induction, and the result is the transfer of low-momentum (blue contoured) fluid away from the wall, shown by the shape of the velocity contours. Through figure 18(*c–e*), the trough on the left becomes shallower, such that $\partial y_{wall}/\partial x > 0$. Over the midpoint of the trough ($z \sim -0.0656$), vectors shows near-wall fluid being advected away from the wall, and the formation of a pair of counter-rotating streamwise vortices. The centres of these vortices rise along with the wall surface. Figure 18(*f–h*) show the crest becoming taller, and the vectors show that the streamwise vortices continue

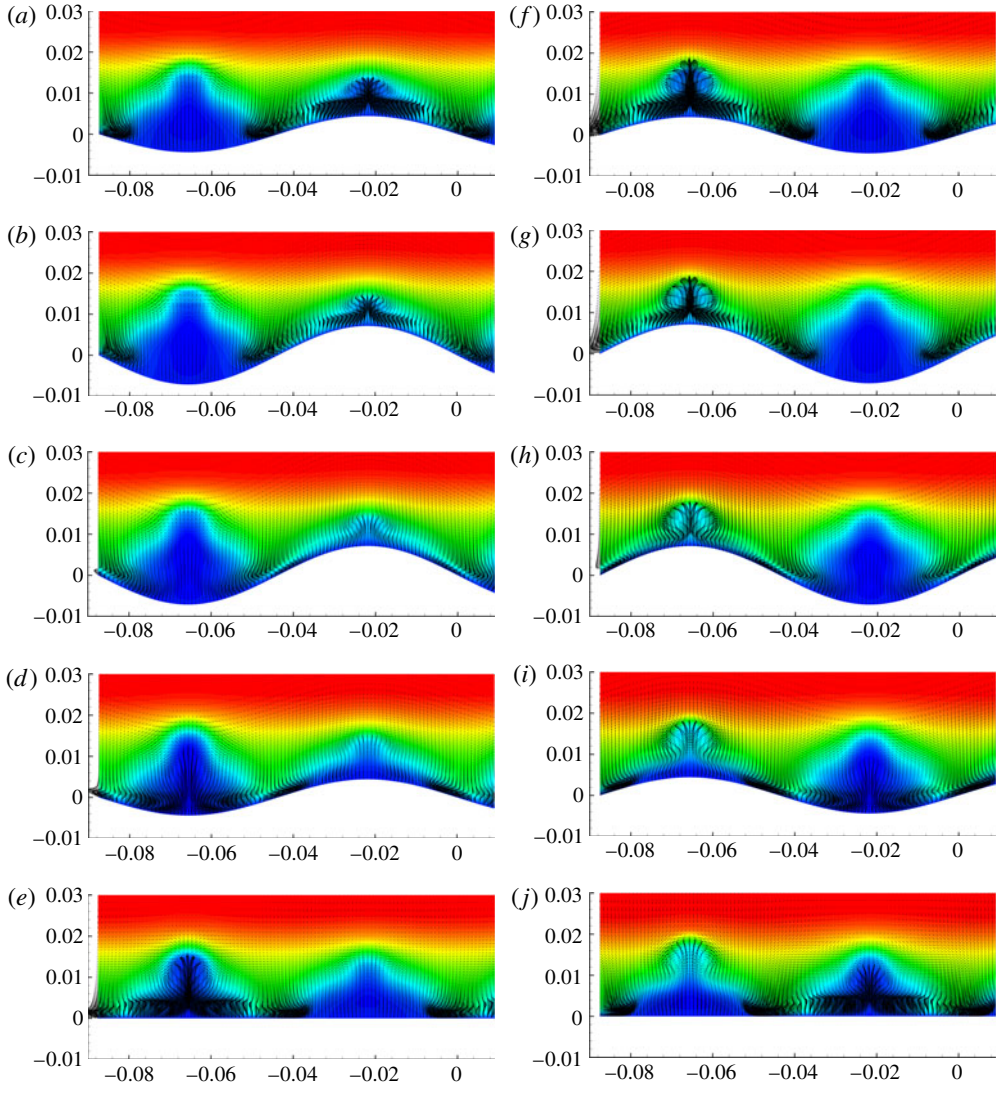

FIGURE 18. (Colour online) Contours of streamwise velocity along with in-plane vectors shown on y–z planes close to each other over a full wavelength of the roughness surface.

to rise. The length of the vectors indicates an increase in their strength. Through figure 18(*h–j*), the roughness crest becomes smaller, $\partial y_{wall}/\partial x < 0$, and the vortices remain at the same physical wall-normal location, effectively farther from the wall. The vectors indicate weakening of the vortices. Similar evolution of the vortices is observed on the right-hand side of the figures ($z \sim -0.022$), though these are not in phase with the formation of vortices on the left. A pair of vortices is observed in figure 18(*a*); they weaken as $\partial y_{wall}/\partial x < 0$ from figure 18(*b–d*) and almost disappear by figure 18(*e*). Another pair begins to form starting at figure 18(*h*) as y_{wall} rises from its minimum.

The present results indicate that the vortices are formed when $\partial y_{wall}/\partial x > 0$, i.e. when the near-wall fluid is being pushed up due to the roughness contours.

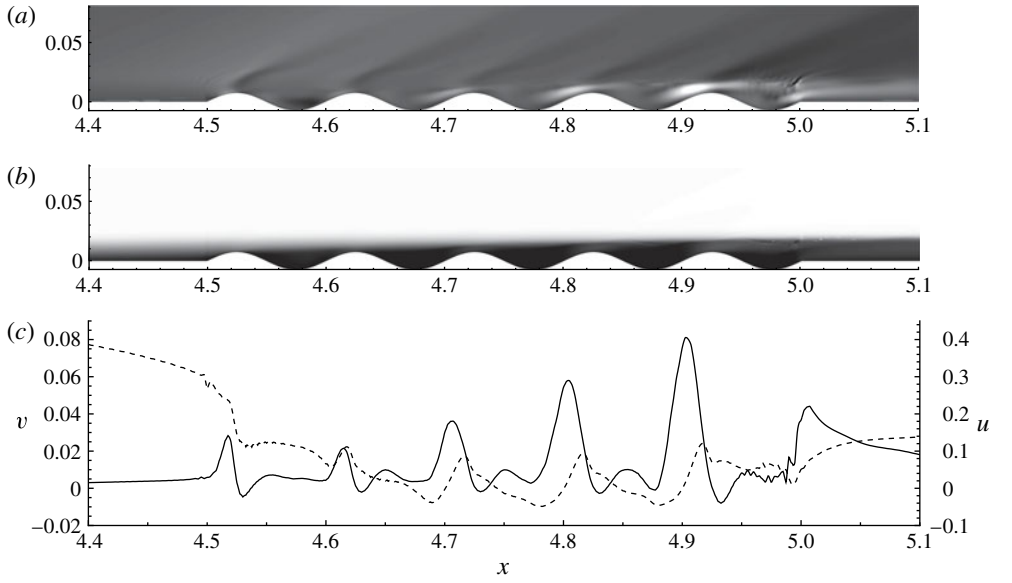

FIGURE 19. (*a*) Contours of v show that fluid possesses upward velocity over the roughness elements. (*b*) Contours of u show the lifting up of the shear layer. (*c*) Profiles of u (dashed) and v (continuous) at $y = 0.008$ show that, as the peak u remains nominally the same, peak v increases over successive roughness elements.

Figure 19 shows contours of streamwise and wall-normal velocities on an x–y plane. Contours of u show the gradual lifting of the shear layer, and contours of v show regions of upward velocity in front of the roughness peaks. Note that the volume of fluid with upward velocity increases with x. Figure 19 also plots u and v as a function of x at a height just over the roughness peaks ($y/k \sim 0.008/0.0075 \sim 1.066$). The profile of u shows a deceleration as the fluid approaches the roughness region and over the first two roughness elements. Thereafter, the profile shows a periodic behaviour of acceleration and deceleration. The profile of v shows a small positive velocity in the laminar flow region, and a periodic variation over the roughness region – an increase in front of the roughness elements and a decrease beyond the peaks. Note that peak vertical velocity increases with successive roughness elements. Figure 20 shows contours of time-averaged wall-normal and spanwise velocities on a wall-parallel plane ($y = 0.005$). These contours show that, earlier on, the motion of the fluid is around the roughness elements, evidenced by the higher magnitude of w and very little v. Successively, contours show little spanwise motion and increasing motion of the near-wall fluid away from the wall. With successive roughness elements, both the extent of upward motion and the magnitude of v increase, consistent with figure 19. It appears that this impulsive upward velocity of the fluid generates the pairs of streamwise vortices, and, as the magnitude of v increases, so does the strength of the vortices.

4.4. *What causes this upward velocity?*

In the absence of roughness elements, inertia dictates that the fluid motion is predominantly horizontal. In the present simulation, the contours of the roughness cause the near-wall fluid to be pushed away from the wall, as can be shown using the wall pressure field. Figure 21(*a*) plots the wall pressure as a function of the

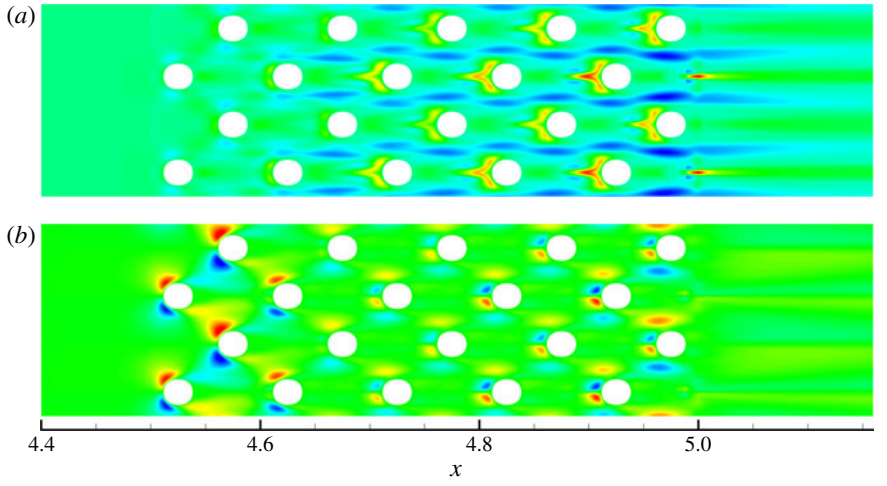

FIGURE 20. (Colour online) Contours of velocity components (*a*) v and (*b*) w on a wall-parallel plane close to the wall ($y = 0.005$). Note that flow is mostly around the roughness elements initially, and over the roughness elements downstream.

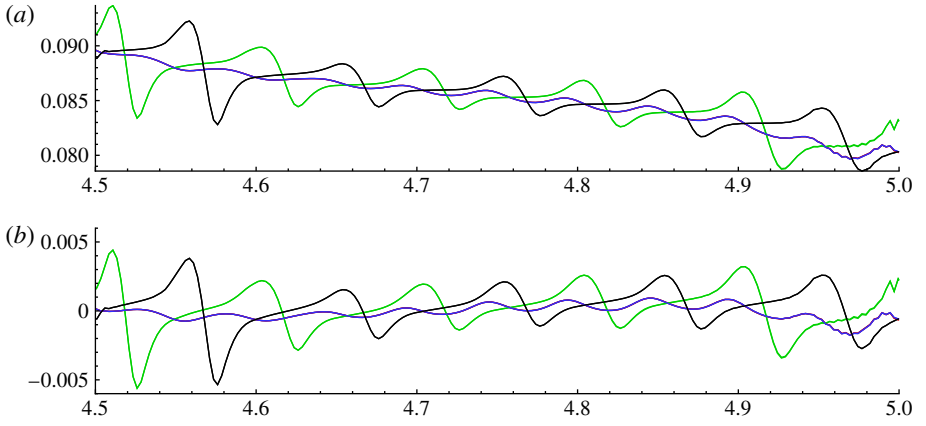

FIGURE 21. (Colour online) Profiles of (*a*) pressure and (*b*) perturbation pressure p_{pert} plotted on the roughness surface along lines shown in figure 11.

downstream distance along lines corresponding to figure 11. The curves show local pressure variations over the roughness element (hence a function of x) along with a steady decrease exhibited at all spanwise locations. The pressure drop can be attributed to the drag on the fluid due to the roughness region. At any x, however, the local variation provides the wall-normal force on the fluid. With this hypothesis, the wall pressure is partitioned as $p = p_{lin} + p_{pert}$, where p_{lin} is a least-squares linear fit to one of the curves in figure 21(*a*), and the perturbation pressure $p_{pert} = p - p_{lin}$ is shown in figure 21(*b*). The upward force on the fluid is $p_{pert} \cdot n_y$, where n_y is the unit normal in the wall-normal direction made by the surface. Figure 22 shows contours of $p_{pert} \cdot n_y$ on the roughness surface. Fluid slows down in front of the roughness element, increasing the pressure. The maximum pressure is observed towards the centre of the roughness element, and is similar to the expected pressure distribution of the flow past

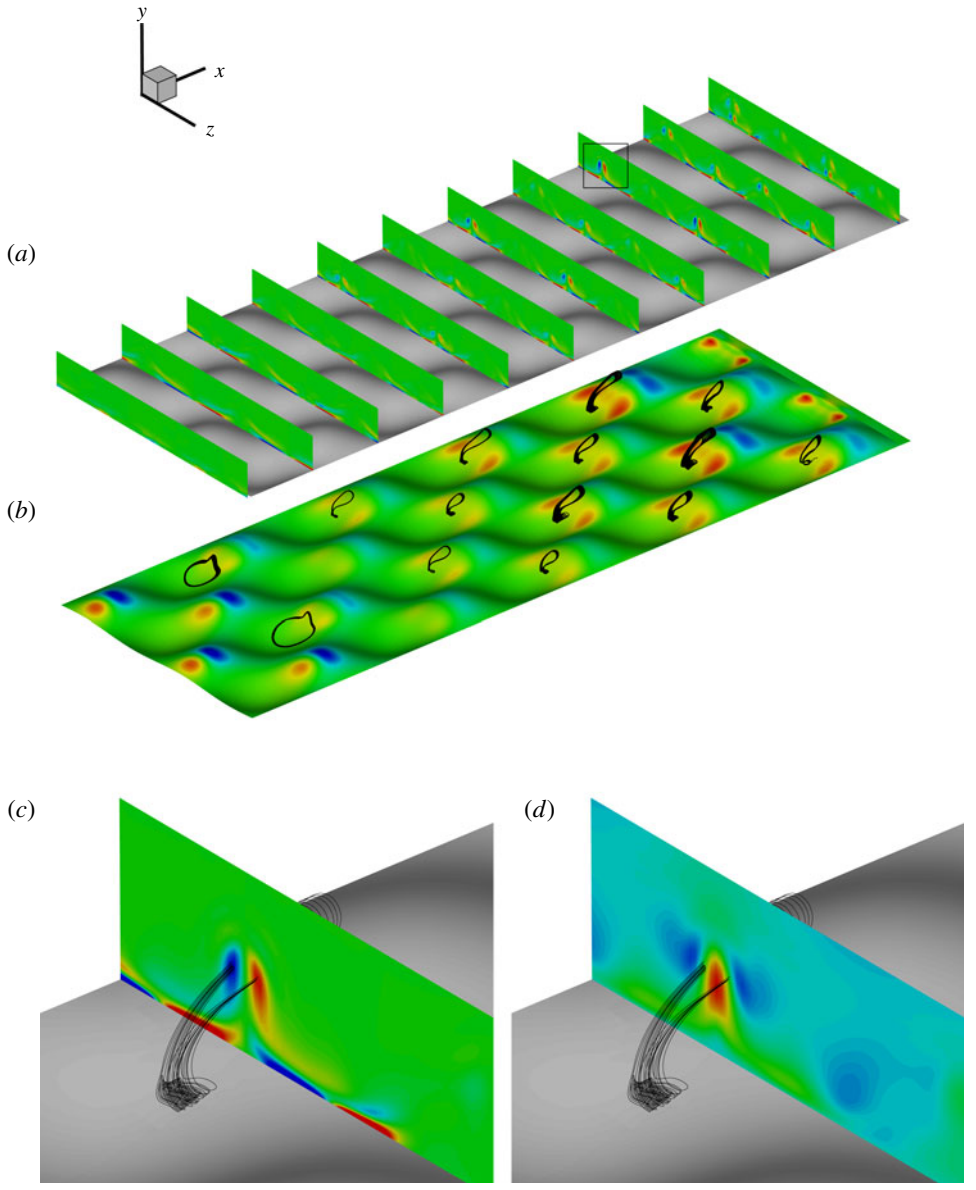

FIGURE 22. (Colour online) (*a*) Contours of ω_x at a few z–y planes along the roughness region. (*b*) Contours of the upward impulse $p_{pert} \cdot n_y$ exerted on the fluid by the roughness elements, along with a few vortex lines. Successive roughness elements exert more impulse on the fluid, generating stronger vortices. (*c*,*d*) One of the z–y planes in greater detail, using contours of ω_x and v.

an obstacle. Past the first roughness elements, the velocity field is no longer uniform in the spanwise direction.

Successive roughness elements exhibit higher $p_{pert} \cdot n_y$ away from their centres and reflect the wake-like velocity field of the fluid approaching them. With increasing x, the magnitude of this upward force increases, along with the area over which it

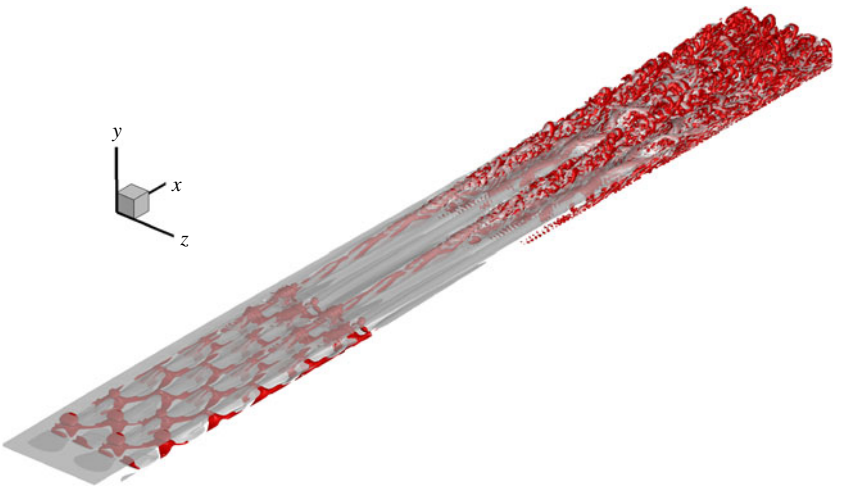

FIGURE 23. (Colour online) Interaction of the roughness-generated vortices with the shear layer shown using an isosurface of vorticity ($\omega_z = -10$) and isosurface of Q criteria ($Q = 40$). The vortices are fairly coherent until they reach the shear layer, and this interaction is followed by a turbulent flow downstream.

is active. This force distribution results in a v velocity in front of, and over, each roughness element, which in turn produces a pair of vortices. Figure 22 also shows representative vortex lines indicating the location of the streamwise vortices, and end views of contours of ω_x indicating the vortex cores. Closer views of one of the end views are also shown, along with contours of ω_x and velocity v. As the fluid moves from a trough to the next crest, the surface exerts an upward force, which results in a vertical velocity v, non-uniform in the span. This 'impulse' produces a pair of streamwise vortices.

In the present simulations, the vortices are fairly steady earlier on, while the ones near the downstream end of the roughness region are unsteady and are shed periodically. As these vortices convect past the roughness region, their mutually induced velocity acts to lift them away from the wall and interact with the shear layer. This interaction causes the shear layer to break down, resulting in the transition to turbulence. Figure 23 shows the interaction between the shear layer (shown using an isosurface of $\omega_z = -10$) and the vortices (shown using isosurfaces of $Q = 40$). Note that the vortices shed behind the roughness elements are initially oriented in the x direction. As they move downstream, the head is more obvious, as is their inclination with respect to the horizontal. The vortices are also very coherent as long as they are under the shear layer. As the vortices reach the shear layer, the coherence is lost, the shear layer breaks up and the isosurfaces indicate a turbulent flow downstream. The vortices leaving the roughness region are characterized by two streamwise legs joined by a head towards the downstream end. However, they appear different from the 'hairpin vortices' associated with turbulent flows. Only as the flow becomes turbulent do we see hairpin vortices. A few such vortices are clearly visible in figure 24, where the head of the vortex is not only higher than the legs but almost vertical and possesses an omega shape (Zhou *et al.* 1999). Note that figure 24 is striking in the coherence and number of hairpins observed, and is very similar to the illustrations in Wu & Moin (2009), where transition is induced by an entirely different

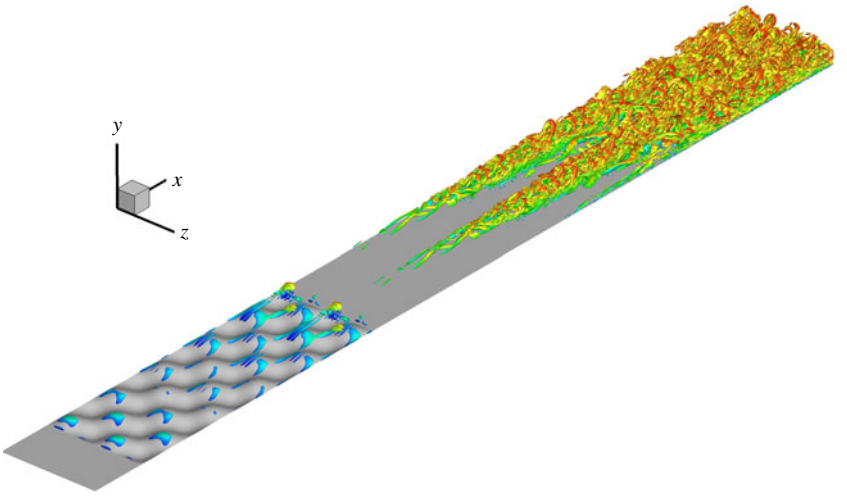

FIGURE 24. (Colour online) Isosurfaces of Q criteria ($Q = 150$) coloured by streamwise velocity u. The figure shows hairpin vortices in the turbulent region.

FIGURE 25. Instantaneous contours of streamwise velocity from simulation 4 in table 2 show that flow remains laminar past the roughness region. Mach number is 2.9, $Re = 635\,000$/inch, and the roughness amplitude $k = 0.005$.

means – packets of isotropic freestream turbulence interacting with an incompressible laminar boundary layer.

5. Simulations at other conditions

The above transition to turbulence had the following components: formation of a (non-planar) shear layer over the roughness surface, formation of streamwise vortices over the roughness elements, unsteadiness of these vortices and their interaction with the shear layer. In the present study, simulations were performed for a few different conditions by varying Mach number, wall temperature, Reynolds number and the roughness height. In all these simulations, the roughness region extended between $x = 4.5$ and 5.0, k_x and k_z were the same, and the origin of the laminar boundary layer is assumed to be at $x = 0$. The computational mesh used for all the simulations was the same, and was based on the grid refinement study for simulation 5. Table 2 lists the relevant parameters for the various simulations, and it can be seen that two of the simulations resulted in flows that did not transition. Figure 25 is a snapshot of one such laminar flow (simulation 4 in table 2) using contours of u. Similar to figure 4, streamwise streaks of alternating high and low velocities are observed. Past the roughness region, however, there are no spanwise perturbations and the flow remains laminar, even as the streaks persist downstream. Between simulations 3 and 4, the only difference is the wall temperature ($1.9\,T_\infty$ versus $2.68\,T_\infty$), and the hotter wall results in a laminar flow.

Simulation	Mach number	k	$k/\delta_{x=4.5}$	T_{wall}/T_∞	Reynolds number (per inch)	Transitional behaviour	Re_{local} $(\rho_{wall}u_\infty k)/\mu_{wall}$	$Re_{roughness}$ $(\rho_\infty u_\infty k)/\mu_\infty$
1	2.25	0.0025	0.136	1.9075	635 000	Laminar	480.85	1587.5
2	2.25	0.005	0.272	1.9075	635 000	Turbulent	961.70	3175
3	2.9	0.005	0.224	1.9075	635 000	Turbulent	961.70	3175
4	2.9	0.005	0.21	2.682	635 000	Laminar	544.24	3175
5	2.9	0.0075	0.304	2.682	635 000	Turbulent	816.36	4762.5
6	2.9	0.005	0.412	2.682	1143 000	Turbulent	979.63	5715

TABLE 2. Sensitivity of transitional behaviour to the various parameters. Reynolds number based on freestream properties does not account for this dependence, which is better captured by a local Reynolds number.

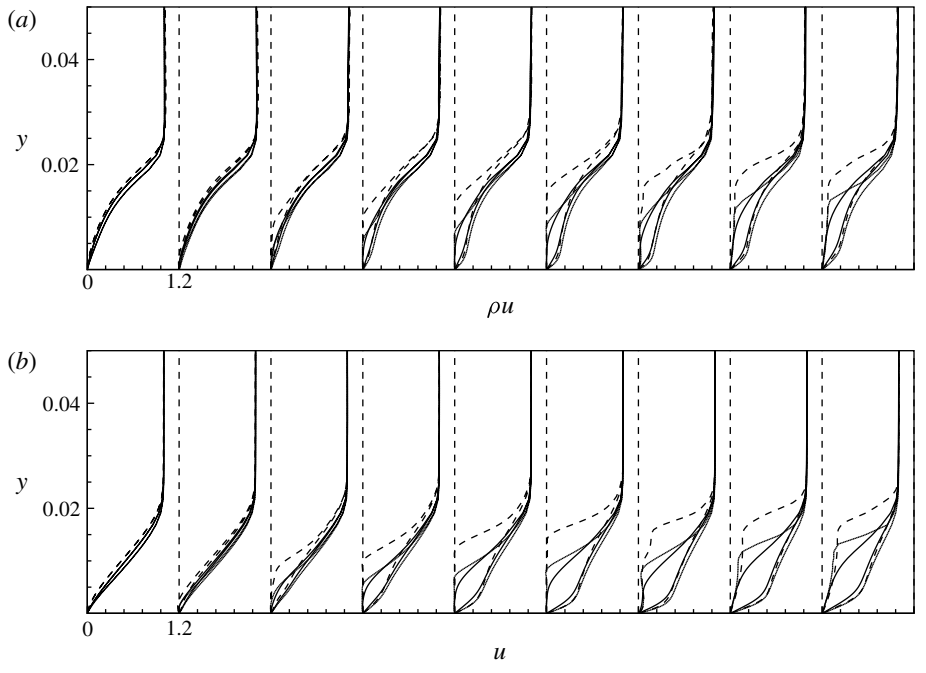

FIGURE 26. Comparison of profiles between different simulations: (*a*) mass flux and (*b*) streamwise velocity u are plotted. The plots correspond to simulation 3 (dotted curve), simulation 4 (continuous curve) and simulation 5 (dashed curve). The flow that does not transition exhibits a smaller gradient/shear.

Figure 26 shows wall-normal profiles of mass flux (ρu) and velocity (u) at a few streamwise locations ($x = 4.475$, 4.5, 4.6, 4.7, 4.8, 4.9, 5.0, 5.1 and 5.2). There is little difference in the profiles upstream of the roughness region. Over the roughness region, the profiles begin to diverge. Near-wall momentum loss begins early for simulation 4 with the largest roughness height. Further downstream, this profile shows a larger y extent of low-momentum fluid. Profiles from simulations 3 and 5 ($k = 0.005$) begin to show differences about midway through the roughness region. In all three cases, profiles exhibit spanwise gradients in the form of accelerated and decelerated profiles. Where the flow does not transition, there is an absence of the steep gradient ($\partial/\partial y$) and the inflection point characteristic of the other two simulations. Since $\rho_{wall} \propto 1/T_{wall}$, where the wall temperature is higher, near-wall momentum is comparatively lower. Hence, from the same roughness surface, increasing the wall temperature results in a smaller near-wall momentum deficit and a weaker shear layer. Along the same lines, larger roughness height results in greater near-wall momentum deficit and a stronger shear, as evidenced by figure 26.

The previous section showed that the streamwise vortices underneath the shear layer play a role in perturbing the shear layer, and causing the flow to transition. Figure 27 shows instantaneous contours of streamwise velocity u on the plane $x = 5.0$ corresponding to the end of the roughness region from simulations 3, 4 and 5. In all the cases, the figure shows near-wall low-momentum fluid directly behind the roughness elements. Visually, the shear layer in simulation 4 is comparatively diffuse, consistent with the velocity profiles in figure 26. The shape of velocity contours (low-momentum fluid) in simulation 4 is very different from that of the other two.

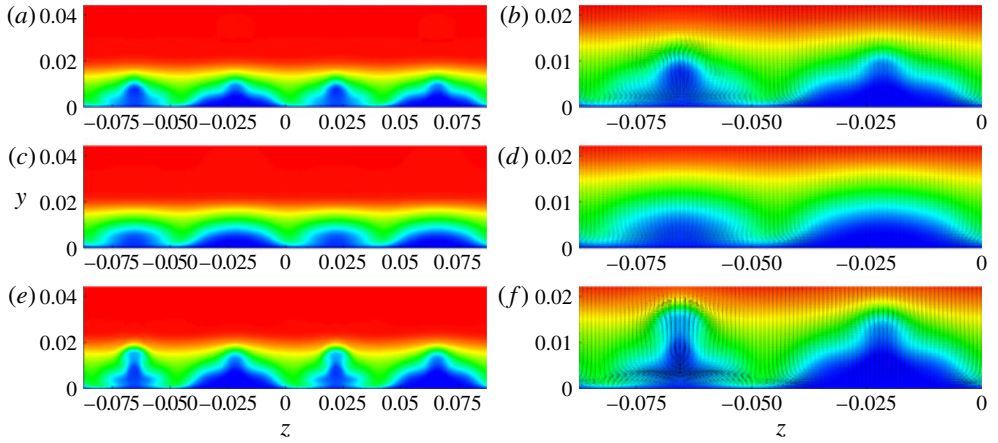

FIGURE 27. (Colour online) Comparison of velocity fields on the plane $x = 5.0$ (end of the roughness region) between simulations 3 (*a*,*b*), 4 (*c*,*d*) and 5 (*e*,*f*). Contours of u show low-momentum fluid behind the roughness elements in all cases. In the case of simulation 4, the velocity gradient across the shear layer is weaker, and the vectors show no appreciable in-plane rotation. The absence of streamwise vortices causes the velocity contours of simulation 4 to look different from the other two.

The presence of a pair of streamwise vortices under the shear layer causes the transfer of low-momentum fluid upwards due to their mutual upwash, resulting in velocity contours as in figure 27(*a*,*c*). The vectors in figure 27 show that simulation 4 does not produce these vortices and, as a result, the velocity contours look different. Hence, it appears that a combination of weaker shear (smaller velocity gradients) and the absence of the vortices (which perturb and steepen the shear) causes the flow in simulation 4 to remain laminar. This behaviour is consistent with the effect of mean shear on the production term ($\overline{\rho u_i'' u_j''}\,\partial \widetilde{u}_i/\partial x_j$, where $\widetilde{u}_i$ is the Favre averaged velocity, and $u_i'' = u_i - \widetilde{u}_i$) of the turbulent kinetic energy equation. It is also qualitatively similar to the expectations from transient growth theory. In contrast to simulation 4, simulations 3 and 5 possess a strong shear as well as the streamwise vortices, and they result in a turbulent flow.

Table 2 lists the roughness Reynolds number for the different simulations, defined as $\rho_\infty u_\infty k/\mu_\infty$. Note that simulations 2, 3 and 4 have the same $Re_{roughness}$ and yet differ in their Mach number and wall temperature, resulting in different transitional behaviour. Since transition is sensitive to the fluid properties in the vicinity of the roughness elements, a local Reynolds number, defined as $\rho_{wall} u_\infty k/\mu_{wall}$, is computed and also listed in table 2. Note that transitional behaviour is consistent with this Reynolds number.

6. Summary

Direct numerical simulations of a Mach 2.9 laminar flow over a distributed roughness region have been performed to study the mechanism of high-speed transition. Roughness causes deceleration of near-wall fluid, resulting in a mixing-layer-like velocity profile, and a curved shear layer over the roughness elements. Roughness also results in pairs of streamwise vortices over the roughness elements. These vortices are formed due to the the upward impulse imparted to the near-wall fluid by the roughness surface, and differ from the flow past a single row of roughness

elements, where the boundary layer vorticity wraps around the roughness element and results in streamwise vortices (horse-shoe vortices). These roughness-generated vortices are unsteady and are shed periodically towards the downstream end of the roughness region. As the vortices advect downstream, their mutually induced velocity moves them away from the wall and towards the shear layer. Their interaction with the shear layer is quickly followed by a transition to turbulence. The mean velocity field in the turbulent region compares well to available data for fully developed turbulent boundary layers. Simulations at different parameters show that, in cases where the shear is not as strong, and where the streamwise vortices are not as pronounced, the flow does not transition. A local Reynolds number based on wall viscosity and density appears to be a better indicator of transition than the Reynolds number based on free stream fluid properties.

Acknowledgements

This work was supported by NASA under the hypersonics NRA program under grant NNX08AB33A. Computer time for the simulations was provided by the Minnesota Supercomputing Institute (MSI).

REFERENCES

ACARLAR, M. S. & SMITH, C. R. 1987 A study of hairpin vortices in a laminar boundary layer. Part 1. *J. Fluid Mech.* **175**, 1–42.

BERRY, S. A., HAMILTON, H. H. II & WURSTER, K. E. 2006 Effect of computational method on discrete roughness correlations for shuttle orbiter. *J. Spacecr. Rockets* **43** (4), 842–852.

BERRY, S. A. & HORVATH, T. J. 2007 Discrete roughness transition for hypersonic flight vehicles. *AIAA Paper* 2007-0307.

BERRY, S. A., HORVATH, T. J., HOLLIS, B. R., THOMPSON, R. A. & HAMILTON, H. H. II 2001 X-33 hypersonic boundary-layer transition. *J. Spacecr. Rockets* **38** (5), 646–657.

BOOKEY, P. B., WYCKHAM, C., SMITS, A. J. & MARTIN, M. P. 2005 New experimental data of STBLI at DNS/LES accessible Reynolds numbers. *AIAA Paper* 2005-309.

CHOUDHARI, M. & FISCHER, P. 2005 Roughness-induced transient growth *AIAA Paper* 2005-4765.

CHOUDHARI, M., LI, F., WU, M., CHANG, C. L., EDWARDS, J., KEGERISE, M. & KING, R. 2010 Laminar–turbulent transition behind discrete roughness elements in a high-speed boundary layer. *AIAA Paper* 2010-1575.

CORKE, T. C., BAR-SEVER, A. & MORKOVIN, M. V. 1986 Experiments on transition enhancement by distributed roughness. *Phys. Fluids* **29** (10), 3199–3213.

EKOTO, I. W., BOWERSOX, R. D. W., BEUTNER, T. & GOSS, L. 2008 Supersonic boundary layers with periodic surface roughness. *AIAA. J.* **46** (2), 486–497.

ELENA, M., LACHARME, J. & GAVIGLIO, J. 1985 Comparison of hot-wire and laser Doppler anemometry methods in supersonic turbulent boundary layers. In *Proceedings of the International Symposium on Laser Anemometry* (ed. A. Dybb & P. A. Pfund). ASME.

ERGIN, F. G. & WHITE, E. B. 2006 Unsteady and transitional flows behind roughness elements. *AIAA J.* **44** (11), 2504–2514.

FEDEROV, A. 2010 Transition and stability of high-speed boundary layers. *Annu. Rev. Fluid Mech.* **43**, 79–95.

GATSKI, T. B. & ERLEBACHER, G. 2002 Numerical simulation of a spatially evolving supersonic turbulent boundary layer. *NASA Tech. Memo.* 211934.

GUARINI, S. E., MOSER, R. D., SHARIFF, K. & WRAY, A. 2000 Direct numerical simulation of a supersonic turbulent boundary layer at Mach 2.5. *J. Fluid. Mech.* **414**, 1–33.

JIMENEZ, J. 2004 Turbulent flows over rough walls. *Annu. Rev. Fluid Mech.* **36**, 173–196.

KLEBANOFF, P. 1955 Characteristics of turbulence in a boundary layer with zero pressure gradient. *NASA Rep.* 1247.

KLEBANOFF, P. S. & TIDSTROM, K. D. 1972 Mechanism by which a two-dimensional roughness element induces boundary-layer transition. *Phys. Fluids* **15** (7), 1173–1188.

LOGINOV, M. S., ADAMS, N. A. & ZHELTOVODOV, A. A. 2006 Large-eddy simulation of shock-wave/turbulent-boundary-layer interaction. *J. Fluid. Mech.* **565**, 135–169.

MASON, P. J. & MORTON, B. R. 1987 Trailing vortices in the wakes of surface-mounted obstacles. *J. Fluid Mech.* **175**, 247–293.

MORKOVIN, M. V., RESHOTKO, E. & HERBERT, T. 1994 Transition in open flow systems: a reassessment. *Bull. Am. Phys. Soc.* **39**, 1–31.

PARK, N. & MAHESH, K. 2007 Numerical and modelling issues in LES of compressible turbulent flows on unstructured grids. *AIAA Paper* 2007-722.

REDA, D. C 2002 Review and synthesis of roughness-dominated transition correlations for reentry applications. *J. Spacecr. Rockets* **39** (2), 161–167.

REDFORD, J. A., SANDHAM, N. D. & ROBERTS, G. T. 2010 Roughness-induced transition of compressible laminar boundary layers. In *Proceedings of the Seventh IUTAM Symposium on Laminar–Turbulent Transition, Stockholm, Sweden, 2009* (ed. P. Schlatter & D. S. Henningson). *Seventh IUTAM Symposium on Laminar-Turbulent Transition, IUTAM Bookseries 18*, pp. 337–342. Springer Science+ Business Media B.V.

RESHOTKO, E. 1976 Boundary-layer stability and transition. *Annu. Rev. Fluid Mech.* **8**, 311–349.

RESHOTKO, E. 2001 Transient growth: a factor in bypass transition. *Phys. Fluids* **13** (5), 1067–1075.

RESHOTKO, E. 2007 Is Re_θ/M_e a meaningful transition criterion? *AIAA Paper* 2007-943.

RESHOTKO, E. 2008 Roughness-induced transition. Transient growth in 3-D and supersonic flow. In *RTO-AVT/VKI Lectures Series, Advances in Laminar–Turbulent Transition Modelling* VKI, Brussels, Belgium, June 2008.

RESHOTKO, E. & TUMIN, A. 2004 Role of transient growth in roughness-induced transition. *AIAA Journal* **42** (4), 766–770.

RINGUETTE, M. J., BOOKEY, P. B., WYCKHAM, W. & SMITS, A. J. 2009 Experimental study of a Mach 3 compression ramp interaction at $Re_\theta = 2400$. *AIAA J.* **47**, 373–385.

ROBERTS, S. K. & YARAS, M. I. 2005 Boundary-layer transition affected by surface roughness and free-stream turbulence. *Trans. ASME: J. Fluids Engng* **127**, 449–457.

SAHOO, D., PAPAGEORGE, M. & SMITS, A. J. 2010 PIV experiments on a rough-wall hypersonic turbulent boundary layer. *AIAA Paper* 2010-4471.

SARIC, W. S., REED, H. L. & WHITE, E. B. 2003 Stability and transition of three-dimensional boundary layers. *Annu. Rev. Fluid Mech.* **35**, 413–440.

SCHLICHTING, H. T. 1963 *Boundary Layer Theory*. McGraw-Hill.

SCHNEIDER, S. P. 2008 Summary of hypersonic boundary-layer transition experiments on blunt bodies with roughness. *J. Spacecr. Rockets* **45** (6), 1090–1105.

SPALART, P. R. 1998 Direct simulation of a turbulent boundary layer up to $Re_\theta = 1410$. *J. Fluid Mech.* **187**, 61–98.

STETSON, K. F. 1990 Comments on hypersonic boundary-layer transition. Wright Research and Development Center, WRDC-TR-90-3057.

TANI, I. 1969 Boundary layer transition. *Annu. Rev. Fluid Mech.* **1**, 169–196.

TUMIN, A. & RESHOTKO, E. 2003 Optimal disturbances in compressible boundary layers. *AIAA J.* **41** (12), 2357–2363.

TUMIN, A. & RESHOTKO, E. 2004 The problem of boundary-layer flow encountering a three-dimensional hump revisited. *AIAA Paper* 2004-101.

VAN DRIEST, E. R. & BLUMER, C. B. 1962 Boundary layer transition at supersonic speeds – three dimensional roughness effects (spheres). *J. Aerosp. Sci.* **29**, 909–916.

VAN DRIEST, E. R. & MCCAULEY, W. D. 1960 Measurements of the effect of two-dimensional and three-dimensional roughness elements on boundary layer transition. *J. Aero. Sci.* **27**, 261–271.

WANG, X. & ZHONG, X. 2008 Receptivity of a hypersonic flat-plate boundary layer to three-dimensional surface roughness. *Journal of Spacecr. Rockets* **45** (6), 1165–1175.

WHITE, E. B. 2002 Transient growth of stationary disturbances in a flat plate boundary layer. *Phys. Fluids* **14** (12), 4429–4439.

WU, M. & MARTIN, M. P. 2007 Direct numerical simulation of supersonic turbulent boundary layer over a compression ramp. *AIAA J.* **45**, 879–889.

WU, X. & MOIN, P. 2009 Direct numerical simulation of turbulence in a nominally zero-pressure-gradient flat-plate boundary layer. *J. Fluid Mech.* **632**, 5–41.

ZHELTOVODOV, A. A., TROFIMOV, V. M., SCHULEIN, E. & YAKOVLEV, V. N. 1990 An experimental documentation of supersonic turbulent flows in the vicinity of forward- and backward-facing ramps. *Tech. Rep.* 2030. Institute of Theoretical and Applied Mechanics, USSR Academy of Sciences, Novosibirsk.

ZHOU, J., ADRIAN, R. J., BALACHANDAR, S. & KENDALL, T. M. 1999 Mechanisms for generating coherent packets of hairpin vortices in channel flow. *J. Fluid Mech.* **387**, 353–396.